Communication

Low-RCS UWB Planar Monopole Array Antenna Based on the Optimized Design of the Conductor Layers

Lei Sang, Ji Xu, Ziyan Liu, Yongfeng Mei, Wei Wang, and Zhongxiang Shen

***Abstract*— Using an optimized design of combining traditional copper (Cu) film and novel phase transition film vanadium dioxide (VO_2), this communication proposes an ultrawideband (UWB) planar monopole array antenna with excellent stealth performance. The VO_2 film exhibits two controllable phases: one with low conductivity of less than 10^3 S/m and the other with high conductivity of more than 10^6 S/m. Since VO_2 has lower conductivity than Cu, antenna designs using this material will have lower radiating efficiency as a tradeoff for reducing the radar cross section (RCS). To optimize this tradeoff, careful antenna shape design, and an innovative combination of using VO_2+Cu films, the RCS can be reduced in a UWB without significantly decreasing the gain of the array antenna. In this work, Cu is applied in the regions supporting high current density, while phase transition VO_2 film is used in areas supporting lower current density. Both the shape and size of the VO_2 film are optimized. Compared with the all-Cu film counterpart, the realized gain of the VO_2+Cu hybrid film array antenna is decreased only by an average of 0.4 dBi, maintaining the same radiation pattern in the working band of 6–9 GHz, while the monostatic RCS is reduced by about 9 dB on average across the UWB of 4–11 GHz.**

***Index Terms*— Monopole antenna, radar cross section (RCS) reduction, ultrawideband (UWB) antenna.**

I. Introduction

With the rapid development of stealth and antistealth technologies, antennas with low radar cross section (RCS) over an ultrawideband (UWB) are in high demand for stealth weapons, including tactical fighter aircraft, tanks, unmanned aerial vehicles, and missiles. So far, five main approaches have been proposed to minimize an antenna's RCS, including shape optimization [1], microwave absorbing materials [2], [3], phase cancellation [4], [5], [6], polarization conversion meta-surfaces (PCM) [7], [8], and coding metasurfaces [9].

While optimizing the antenna shape and adding microwave-absorbing materials are the most straightforward approaches to minimizing an antenna's RCS, several drawbacks are apparent. By reducing the number of edges and corners of an antenna, the incident waves are scattered toward directions other than the direction of incidence [10]; however, this method requires the object's shape to be electromagnetically and aerodynamically co-optimized, severely constraining design flexibilities. On the other hand, while a wide range of materials, including lossy materials [11], resonant elements [12], and polymer composites, can serve as microwave absorbers, they may bring undesirable side effects, such as significantly reducing the antenna gain.

The basic operating principle of phase cancellation is to control the reflected waves so as to interfere with the primary incident waves destructively. The reflecting plate may be artificial magnetic conductors (AMCs) [13], electromagnetic band gap structures (EBGs) [14], or perfect electric conductors (PECs) [15]. The drawbacks of this method are that the reflecting plate is usually much larger than the antenna, taking too much space, while the achieved bandwidth is typically not wide enough. In the PCM method, many polarization rotation unit cells are introduced around the antenna to change the polarization rotation ratio of the radiated electromagnetic waves so that the scattered energy is dispersed and the backscattering RCS is reduced. In 2014, Cui et al. [16] proposed the concept of "coding meta-materials" and used 1- and 2-bit coding meta-surfaces for RCS reduction. Then, in [17], multibit coding meta-surfaces were designed for diffusion purposes in the terahertz band. In [18], [19], and [20], two AMCs with 180° out of phase reflection coefficients were selected as the 0 and 1 elements for the 1-bit coding metasurface. The main limitations of the PCM and coding metasurfaces are the large areas required and their selective RCS reduction with respect to the incident angle.

This communication explores a phase transition material applied in antennas and arrays to maintain their good radiation performance while reducing their RCS over a wide frequency range. As a phase transition material, vanadium dioxide (VO_2) film has the remarkable ability to reversibly switch the order of magnitude of its electrical conductivity based on its crystallographic phase. The material has electric conductivity that can be lower than 10^2 S/m in one state (Phase I) and can reach $\sim 10^6$ S/m in the other state (Phase II). Therefore, VO_2 film can be potentially very useful for reducing the RCS of UWB antennas and arrays.

The phase transition of VO_2 films can be triggered by infrared radiation, applied voltage, or heating. For practical implementations, the heating method is used in this work. The phase transition threshold temperature is about 68 °C and can be adjusted by doping [21], [22]. A 2×4 monopole array antenna is designed using a combination of VO_2 film and copper (Cu) film. For comparison, an all-Cu array antenna is also fabricated and measured (Au and Ti films are also used for improving adhesion in the fabrication). Compared to the all-Cu monopole array antenna, the radiation performance of the hybrid array antenna using VO_2+Cu film does not appreciably change, whereas its average monostatic RCS is reduced by more than 9 dB from 4 to 11 GHz.

II. Low-RCS UWB Array Antenna Using VO_2 Film

A. Basic Requirements of the Phase Transition VO_2 Film

To achieve tuning performance, the employed VO_2 film should have the following characteristics.

Manuscript received 17 June 2022; revised 22 December 2022; accepted 2 January 2023. Date of publication 28 February 2023; date of current version 7 April 2023. This work was supported by the National Key Research and Development Program of China under Grant 2021YFA0715301. *(Corresponding author: Wei Wang.)*

Lei Sang, Ji Xu, and Ziyan Liu are with the School of Microelectronics, Hefei University of Technology, Hefei 230601, China.

Yongfeng Mei is with the Department of Materials Science, Fudan University, Shanghai 200433, China.

Wei Wang is with the East China Research Institute of Electronic Engineering, Hefei 230088, China (e-mail: Shu00ww@163.com).

Zhongxiang Shen is with the School of Electrical and Electronic Engineering, Nanyang Technological University, Singapore 639798.

Color versions of one or more figures in this communication are available at https://doi.org/10.1109/TAP.2023.3247905.

Digital Object Identifier 10.1109/TAP.2023.3247905

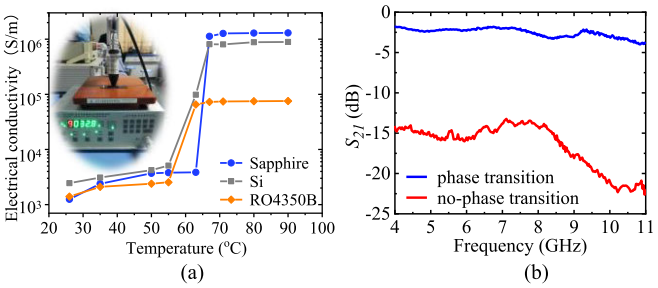

Fig. 1. (a) Temperature-dependent conductivity curves of the VO_2 film on Sapphire, Si, and Duroid RO4350B substrates, respectively (the embedded photo is the conductivity test scene). (b) Frequency-dependent S_{21} curves of the VO_2 microstrip transmission line on a sapphire substrate.

1) In one state (Phase I), the conductivity of the VO_2 film must be as low as possible and no more than 10^3 S/m.

2) In the other state (Phase II), the conductivity of the VO_2 film must be as high as possible and no less than 10^6 S/m.

3) The switching speed between these two states must be as fast as possible, like faster than 200 ns.

4) The triggering mechanism for the phase transition must be as simple as possible.

To satisfy these requirements, the substrate material should be appropriately selected, and the fabrication process must also be optimized accordingly. Typical microwave substrate materials are sapphire, silicon, and composite resin. The conductivity versus temperature characteristics of a 3 × 4 mm VO_2 film of thickness 1.5 μm on different substrates is measured by the four-probe method and compared in Fig. 1(a). For Sapphire, Si, and Rogers Duroid substrates, the VO_2 film's conductivities are 1.5×10^3, 2.3×10^3, and 1.6×10^3 S/m in Phase I, and 2.6×10^6, 0.9×10^6, and 0.8×10^5 S/m in Phase II, respectively. The sapphire substrate enables the VO_2 film to achieve the largest conductivity change ratio, defined as the conductivity in Phase II divided by the conductivity in Phase I, and is, therefore, chosen as the microwave substrate for the antenna design reported in this communication.

The S-parameters of a 50 Ω, 20 mm long microstrip transmission line, fabricated using 1 μm thick VO_2 film as the signal line and 1 μm thick Cu layer as the ground plane, are measured by an N5242 Keysight vector network analyzer from 4 to 11 GHz to demonstrate the significant conductivity variation following the phase transition with an acceptable ohmic loss. As shown in Fig. 1(b), the insertion loss difference is over 12 dB between Phases I and II.

B. Antenna Elements Based on VO_2 Film

Without loss of generality, a planar UWB monopole antenna is considered, as shown in Fig. 2(a). Like a conventional monopole antenna, a tapered microstrip line and cross-etching grooves in the ground surface are both used for impedance matching. The ripples on the radiation patch are used to expand the operating bandwidth in the low-frequency band. HFSS 2020 is used to simulate the antenna.

The antenna has two working states following the two phases of the VO_2 film: low conductivity and high conductivity. When the VO_2 film is in Phase II, its conductivity is close to that of the lead (Pb), so the antenna can operate as a regular UWB monopole antenna in the radiating state. When the VO_2 film is in Phase I, its conductivity is about 1000 times lower than that of Pb, so the antenna's radiation efficiency drastically degrades due to the intentional introduction of high ohmic losses. Therefore, the antenna's RCS will be much lower in this state than in the radiation state.

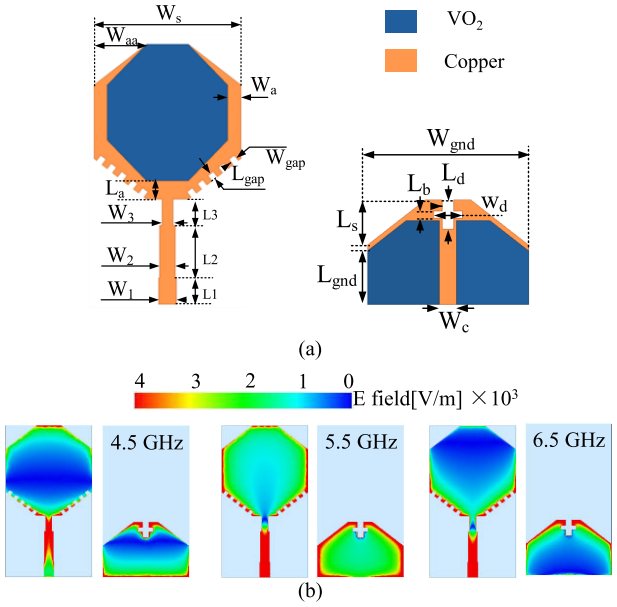

Fig. 2. (a) Shape and critical dimensions of the planar monopole antenna. (b) Simulated electric field distribution at three frequency points.

As the conductivity of the VO_2 film in Phase II is nearly 20 times lower than the conductivity of CU, its ohmic loss will be higher than that of the Cu film. Therefore, the realized antenna gain will decrease proportionally to the increase of VO_2 film used to replace Cu film. On the other hand, for RCS reduction, as the conductivity of the VO_2 film is about 2×10^3 times lower than that of Cu in Phase I, the replacement of Cu using VO_2 can proportionally reduce an antenna's RCS. Therefore, a tradeoff in the proportion of Cu versus VO_2 area should be considered in the antenna design.

To better understand the design tradeoffs, the position and area of the Cu part replaced by the VO_2 film are analyzed. As shown in Fig. 2(b), the electric field of the monopole antenna is mainly concentrated on the feeding portion and around the edge of the radiation patch. Therefore, the Cu area may be replaced by the VO_2 according to the electric field distribution in the regions with low current density. In Fig. 2(a), W_a and L_a mainly determine the area of the VO_2 film. The influence on the realized gain and VSWR are shown in Fig. 3. It can be seen from the simulation results that the area ratio of VO_2/Cu in the radiation structure has little influence on the antenna's VSWR, indicating that a good matching is guaranteed. The impact of the area ratio on the realized gain is more prominent and meets our expectations, where a larger VO_2 area translates to a lower antenna gain.

Furthermore, the realized gain and monostatic RCS as a function of the area ratio between the VO_2 film and Cu film are evaluated at 7.5 GHz, as shown in Fig. 4(a). It can be seen that when the area ratio of VO_2/Cu is about 4.5, the monostatic RCS can be reduced by over 14 dB from the all-Cu baseline while the realized gain is maintained. By setting up the area ratio to 4.5, the S_{11} curves between the all-Cu antenna and VO_2+Cu hybrid antenna are compared in Fig. 4(b). The reflection coefficient S_{11} of the antenna element is lower than –10 dB within 6–9 GHz, which meets the antenna array's 6–9 GHz operating band requirements. Only slight differences exist between the S_{11} parameters of the all-Cu and VO_2+Cu hybrid antennas. The key dimensions of the VO_2+Cu hybrid antenna are listed in Table I.

To examine the RCS reduction performance more comprehensively, the monostatic RCS of the all-Cu and hybrid VO_2+Cu antennas are compared from 4 to 11 GHz, as shown in Fig. 5(a). We define ΔRCS

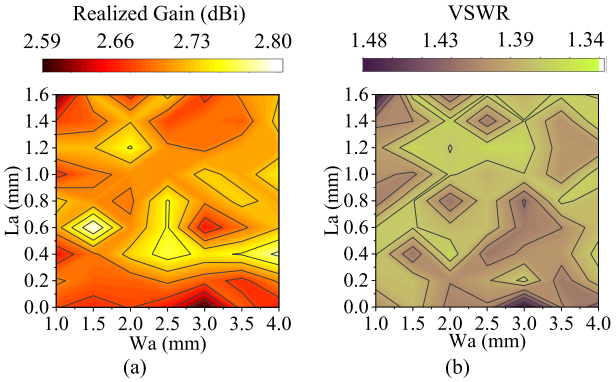

Fig. 3. Dependence of (a) gain and (b) VSWR of the antenna on W_a and L_a at 7.5 GHz.

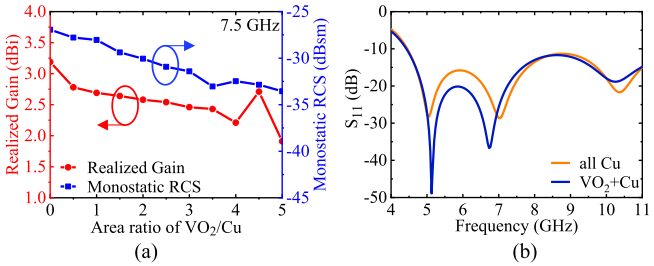

Fig. 4. (a) Realized gain and monostatic RCS (0° incidence) as functions of the VO_2/Cu area ratio at 7.5 GHz. (b) Dependence of the reflection coefficient S_{11} on the frequency.

TABLE I

DIMENSIONS OF THE HYBRID VO_2+CU ANTENNA(DEFAULT UNIT: MM)

W_s	W_{aa}	W_{gnd}	W_{gap}	L_{gap}	L_a	W_3	L_3	L_{gnd}	$H_{sapphire}$
11.2	3.1	0.5	0.5	0.5	0.8	4	2	2.3	0.5
W_2	L_2	W_1	L_1	W_c	L_d	W_d	L_b	L_s	VO_2/Cu THK
0.85	2	1.35	1.2	1.38	2	2	0.5	4	1.5 μm/1.5μm

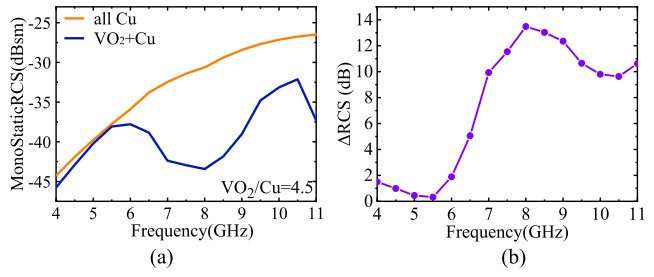

Fig. 5. (a) Comparison of the monostatic RCS (0° incidence) between the all-Cu antenna and the hybrid antenna as a function of frequency. (b) ΔRCS as a function of frequency.

as the difference between the monostatic RCS of the all-Cu monopole and the monostatic RCS of the hybrid VO_2+Cu monopole antenna, as shown in (1). The simulated ΔRCS result is shown in Fig. 5(b) as a function of frequency from 4 to 11 GHz

$$\Delta\text{RCS} = \text{RCS}_{(\text{all}-\text{Cu film antenna})} - \text{RCS}_{(\text{VO2}+\text{Cu film antenna})}. \quad (1)$$

C. Low-RCS Array Antenna

From the practical point of view, most modern weapons and equipment use array antennas. Therefore, based on the hybrid monopole antenna, we further design a 2 × 4 array antenna. The 3-D model of the array is shown in Fig. 6. The transverse and longitudinal spacings between array elements are S_a = 16.6 mm, and S_{ar} = 9 mm, respectively. The length L_{ar} and width W_{ar} of the sapphire substrate are 23 and 66.6 mm, respectively. The array antenna with all-Cu film elements is also simulated for comparison.

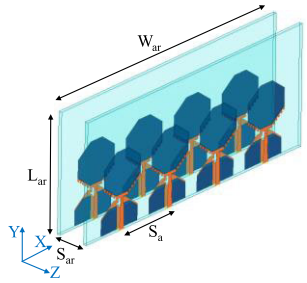

Fig. 6. Three-dimensional model of the 2 × 4 hybrid film array antenna.

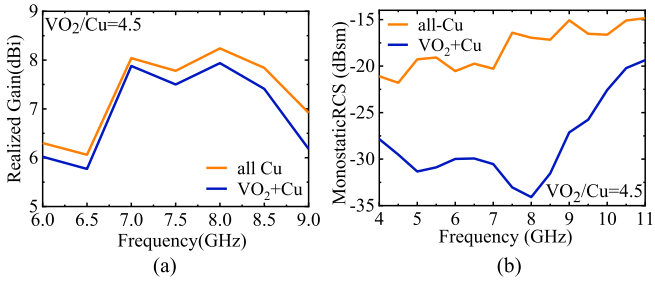

Fig. 7. Performance comparison between the all-Cu array antenna and the hybrid array antenna with an area ratio of 4.5. Comparison of (a) simulated gain and (b) monostatic RCS with 0° incident angle.

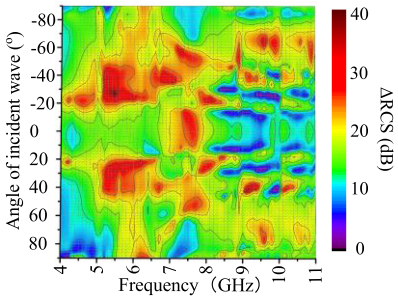

Fig. 8. ΔRCS as a function of frequency and azimuth incident angle.

A comparison of the simulation results between the all-Cu array antenna and hybrid VO_2+Cu array antenna is shown in Fig. 7(a) and (b). Fig. 7(a) compares the simulated realized gains of the two array antennas as a function of frequency. It can be seen that for the case of a VO_2/Cu area ratio at 4.5, the simulated gain of the hybrid antenna is slightly lower compared to the all-Cu array antenna, by a maximum of 0.7 dBi at 9 GHz and by an average of 0.4 dBi from 6 to 9 GHz. Fig. 7(b) compares the monostatic RCS of the two antennas as a function of frequency. The RCS of the VO_2+Cu hybrid array antenna is reduced significantly across the wide frequency band from 4 to 11 GHz, with an average RCS reduction of more than 14 dB.

Compared with the all-Cu array antenna, the RCS reduction effect of the hybrid VO_2+Cu array antenna with different incident angles from 4 to 11 GHz is shown in Fig. 8. It can be seen that over the entire ultrawide frequency band and with varying incident angles, the RCS of the hybrid VO_2+Cu array antenna is reduced significantly. The average RCS reduction is more than 14 dB.

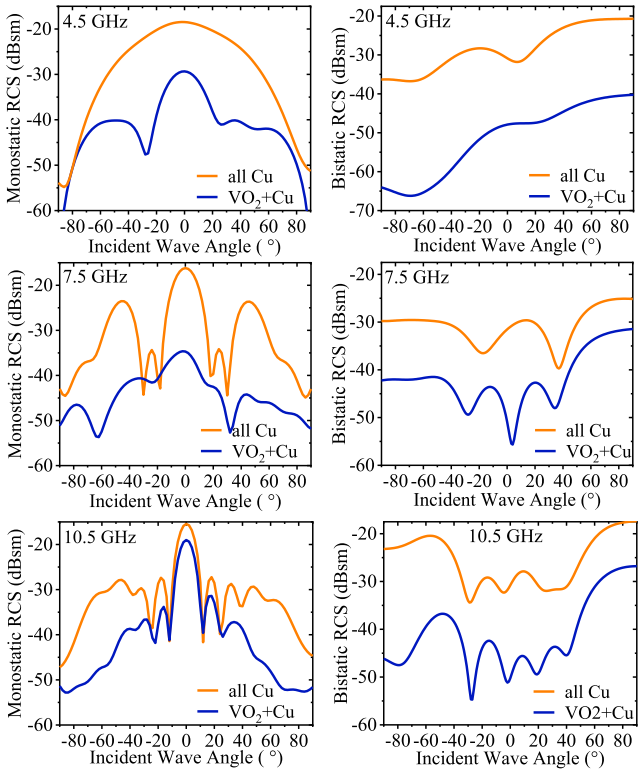

Fig. 9. RCS performance comparisons between the all-Cu array antenna and the hybrid film array antenna under different azimuth angles.

The monostatic RCS and bistatic RCS results under different incident angles were simulated to analyze and verify the radiation performance and RCS reduction performance of the array antenna using the hybrid VO2+Cu film. As shown in Fig. 9, three frequency points are selected to compare the monostatic RCS and bistatic RCS of the conventional all-Cu array antenna and hybrid VO_2+Cu array antenna. It can be seen that the monopole array antenna has both a remarkably lower monostatic-RCS and bistatic RCS by using the VO_2 film. As the surface current varies with the angle of incidence of the electromagnetic wave, the RCS introduced by the surface current also varies with the angle.

III. Fabrication and Measurements

In this communication, a rectangular single-crystal sapphire wafer is used as the substrate to realize the desired VO_2 phase transition characteristics. The VO_2 thin film is deposited by direct-current magnetron sputtering with a high-purity vanadium target. The growth pressure, Ar/O_2 gas flow, D.C. power, and temperature are 11.5 mTorr, 60/40 sccm, 200 W, and 580 °C–700 °C, respectively. The VO_2 phase transition is measured to occur abruptly when the temperature surpasses 68 °C. Simultaneously, the D.C. electrical conductivity increases by over three orders of magnitude from $\sim 1.5 \times 10^3$ to $\sim 2.6 \times 10^6$ S/m.

Because of its compatibility with conventional semiconductor processing, Cu, deposited by E-beam evaporation, is used as the primary conductive material. The Cu layer is patterned to cover the most current-dense region. To increase the adhesion between the Cu and sapphire substrate, a thin layer of Ti with a thickness of about 0.2 μm is initially evaporated in the area where Cu is required, as shown in Fig. 10(a) and (b). Then, to avoid the oxidation of Cu in the air, a gold (Au) thin film with a thickness of 0.3 μm is deposited by E-beam evaporation to fully cover the surface of the Cu region

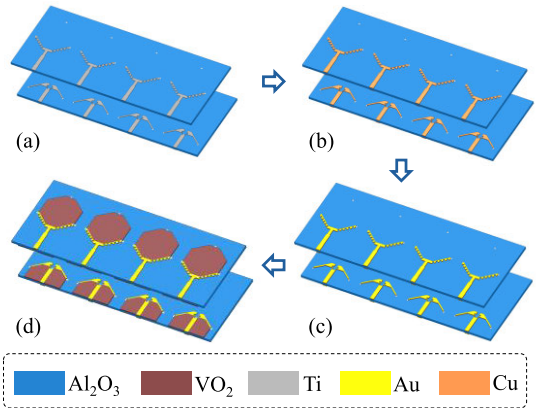

Fig. 10. Layout and fabrication process flow of the VO_2-based array antenna. (a) Single crystal sapphire with the evaporated Ti adhesion layer. (b) E-beam evaporation of a 1.5 μm Cu thin film on both sides of the sapphire substrate. The top Cu layer was patterned with a shadow mask during evaporation. (c) 0.3 μm Au thin film was deposited by E-beam evaporation to cover the top of the Cu thin film on both sides of the sapphire substrates with a shadow mask during evaporation. (d) 1.5 μm VO_2 thin film was sputtered locally onto the top side of the sapphire substrate with a shadow mask during sputtering.

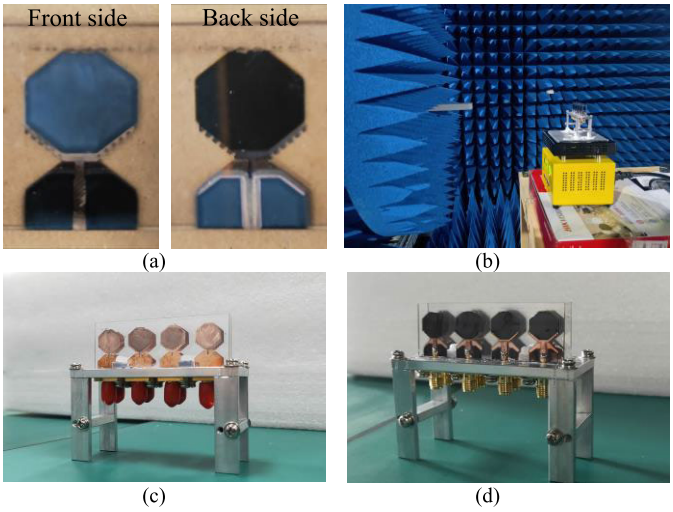

Fig. 11. (a) Optical photograph of the hybrid monopole patch antenna. (b) Planar near-field test apparatus of the array antenna. (c) Assembled array antenna for radiation performance testing (c) all-Cu and (d) VO_2+Cu.

on both sides, as shown in Fig. 10(c). A shadow mask is used to cover the top side of the device during sputtering. Finally, a VO_2 thin film with a thickness of 1.5 μm is sputtered locally onto the sapphire substrate, as shown in Fig. 10(d), and with a shadow mask covering both sides of the device during sputtering.

Fig. 11(a) shows an optical photo of the hybrid VO_2+Cu monopole antenna, in which the blue-black material represents the VO_2 thin film, and the bronze part is the metal film. To facilitate the test, the antenna array on the testing platform, as shown in Fig. 11(b). The inner conductor of the 2.92 mm connector is bonded to the feeding microstrip line by a conductive adhesive. The radiation performance of the antenna is tested by a planar near-field system. The whole antenna is placed on a temperature-controlled platform, and the temperature is raised to 90 °C to ensure Phase II of the VO_2 film, as shown in Fig. 11(c) and (d).

To test the antenna's RCS, the previously described platform is removed, as shown in Fig. 12, and a far-field rotating platform is used. The RCS of each angle is calculated based on the measured S-parameters by using the time window filtering algorithm.

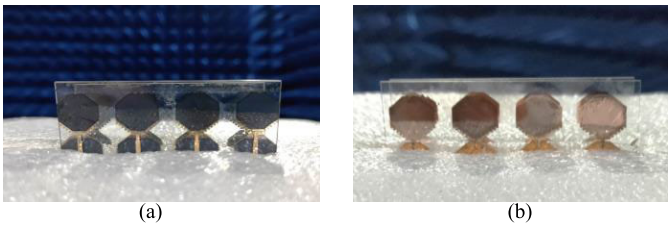

Fig. 12. Array antenna for RCS test. (a) Front side of VO_2+Cu array antenna. (b) Back side of the all-Cu array antenna.

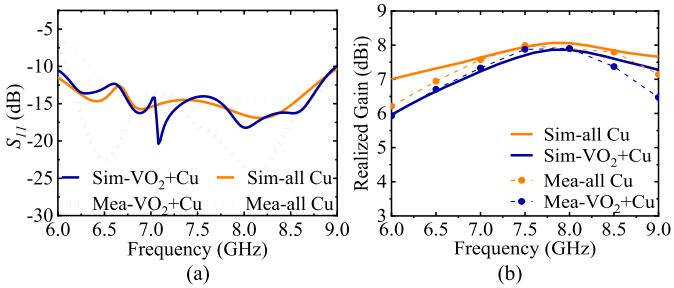

Fig. 13. Performance comparisons between the all-Cu array antenna and the hybrid film array antenna. (a) Comparisons of the S_{11}. (b) Comparisons of the measured realized gain.

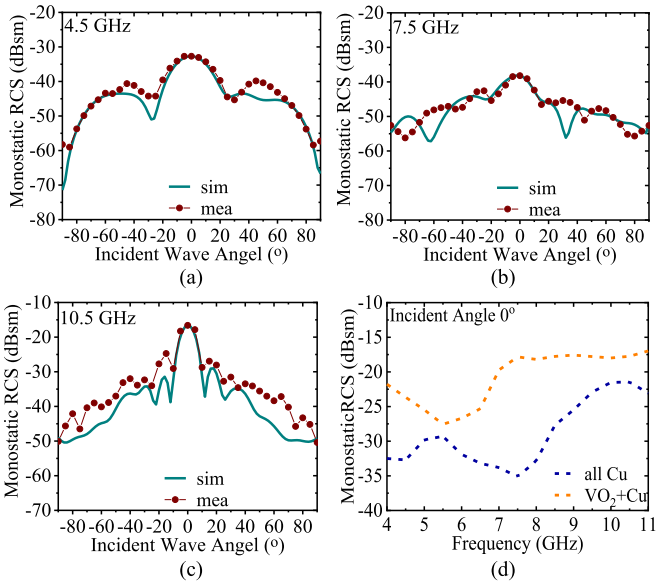

Fig. 14. Comparison of the monostatic RCS dependent with azimuth incident angles at (a) 4.5, (b) 7.5, and (c) 10.5. (d) Comparison of the monostatic RCS between the all-Cu array antenna and the hybrid array antenna dependent on the frequency at 0° incidence angle.

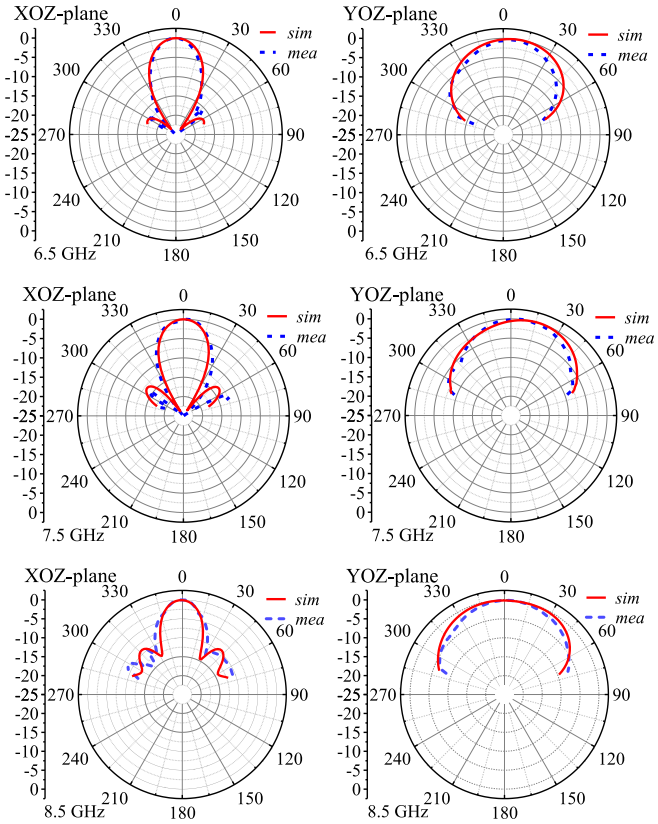

Fig. 15. Comparisons between the simulated and measured radiation patterns (the XOZ plane ($\varphi = 0°$) is the E-plane, and the YOZ plane ($\varphi = 90°$) is the H-plane. In the pattern, the angle is the elevation angle).

It should be noted that when the antenna is in the nonradiation state, the VO_2 film is in Phase I with no need for feeding and heating and with the platform and fixture removed. Therefore, the RCS performance of the array antennas can be tested directly with the standard horn antennas without being affected by the heating platform and fixture.

The measured results of the all-Cu array antenna and hybrid array antenna are shown in Fig. 13. Fig. 13(a) compares the simulated and measured $|S_{11}|$ results between these two array antennas. It can be seen that the measured operating frequency band of the hybrid antenna is from 6 to 9 GHz, which is consistent with the simulated value. Fig. 13(b) compares the measured gain of these two array antennas. The measured gain of the hybrid array antenna is slightly lower than that of the traditional all-Cu array antenna, but the difference is marginal. Measured results show that the maximum reduction of the realized gain reaches about 0.7 dB at 9 GHz, which is consistent with the trend of the simulation results. A noticeable discrepancy between the simulated result and measured data is, however, observed in all performance metrics, which can be attributed to the manual welding of the SMA connectors and unexpected thickness variations of the VO_2 thin films.

Fig. 14(a)–(c) compares the monostatic RCS results of the two array antennas at 4.5, 7.5, and 10.5 GHz as a function of the incident angles. The strong RCS reduction effect of the hybrid array antenna is evident for most incident angles.

The measured RCS results of the two array antennas are compared in Fig. 14(d) in the UWB range from 4 to 11 GHz, where the monostatic RCS reduction of the hybrid array antenna is substantial. The average RCS reduction across the whole frequency band is about 9 dB. As shown in Fig. 2(b), the electric field on the patch is denser at 5.5 GHz, which probably results in the larger RCS around that frequency.

The simulated and measured radiation patterns at three frequency points of the VO_2+Cu hybrid array are compared in Fig. 15. Since a planar near-field testing apparatus is used, the measured data are valid in $\pm 70°$ range. Because of the antenna elements arranged along the X-axis, the pattern in the XOZ plane shows a narrower beamwidth than that in the YOZ plane. It can be seen that the measured patterns differ slightly from the simulated results, which may be due to the inconsistency of soldered joint and the imperfect power-splitting network.

To evaluate the RCS reduction more comprehensively, we compare the antenna's performance with other RCS-reduced antennas published in recent years, as shown in Table II. It can be seen

TABLE II
COMPARISON OF THE PROPOSED ANTENNA WITH OTHER DESIGNS

Ref.	Antenna BW	Antenna Gain/Realized Gain	Monostatic RCS reduction BW	Average Monostatic RCS Reduction	Planar Size (λ)
[3]	5.41-6.25 GHz	5.5 dBi (5.6GHz)	5.2-6.8 GHz (27%)	6.1 dB	1.87×1.87 (5.8GHz)
[6]	4.42-4.57 GHz	NG	6.25-12 GHz (35%)	12 dB	0.93×0.93 (4.5GHz)
[7]	4.2-4.55 GHz	6.44 dBi (4.4GHz)	3.5-5.7 GHz (48%)	13.5 dB	1.75×1.75 (4.4GHz)
[9]	4.92-5.15 GHz	21.8 dBi (5GHz)	4.4-6 GHz (43%)	7 dB	5.92×5.92 (5GHz)
[14]	4.8-7 GHz	13 dBi (5.6GHz)	4.7-5.8 GHz (17%)	6 dB	1.81×1.81 (5.9GHz)
[18]	5.42-5.84 GHz	9.2 dBi (5.6GHz)	4-8 GHz (66%)	6 dB	3.67×3.67 (5.6GHz)
[19]	5.48-5.84 GHz	9.39 dBi (5.6GHz)	4.95-7.18 GHz (36.7%)	6 dB	3.66×3.66 (5.6GHz)
This Work	6-9 GHz	7.7 dBi (7.5GHz)	4-11 GHz (93%)	9 dB	1.67×0.57 (7.5GHz)

that the antenna designed with VO_2 exhibits better RCS reduction performance and has a broader frequency band.

IV. CONCLUSION

A phase transition film has been used to reduce the RCS of a UWB array antenna. Considering the phase transition characteristics of the VO_2 film and the current distribution of a monopole antenna, VO_2 and Cu films have been used together to design a 2×4 array antenna. Compared to an all-Cu film array antenna, the hybrid VO_2+Cu film array antenna has achieved a remarkable RCS reduction over a UWB under a large incidence angle range. The average reduction of the monostatic RCS has been proven to be about 9 dB. The realized gain of the hybrid film array antenna has been measured to be less than 0.7 dBi lower than the all-Cu counterpart. Nearly identical radiation patterns to the all-Cu antenna have been observed.

When the antenna array is in practical use, there are many ways to control the temperature to enable the phase transition. For example, if the array antenna is placed on a fixture, the temperature can be controlled by heating the fixture. Most of the fixtures can readily handle 80 °C. In addition, since the sapphire has acceptable thermal conductivity, the temperature of the array antenna can also be controlled by a thermal-conductivity wire connected to a heat sink.

REFERENCES

[1] X. Ding, Y.-F. Cheng, W. Shao, and B.-Z. Wang, "Broadband low-RCS phased array with wide-angle scanning performance based on the switchable stacked artificial structure," *IEEE Trans. Antennas Propag.*, vol. 67, no. 10, pp. 6452–6460, Oct. 2019.

[2] J. Yu, W. Jiang, and S. Gong, "Wideband angular stable absorber based on spoof surface plasmon polariton for RCS reduction," *IEEE Antennas Wireless Propag. Lett.*, vol. 19, no. 7, pp. 1058–1062, Jul. 2020.

[3] J. Ren, S. Gong, and W. Jiang, "Low-RCS monopolar patch antenna based on a dual-ring metamaterial absorber," *IEEE Antennas Wireless Propag. Lett.*, vol. 17, no. 1, pp. 102–105, Jan. 2018.

[4] Y. Liu, Y. Jia, W. Zhang, Y. Wang, S. Gong, and G. Liao, "An integrated radiation and scattering performance design method of low-RCS patch antenna array with different antenna elements," *IEEE Trans. Antennas Propag.*, vol. 67, no. 9, pp. 6199–6204, Sep. 2019.

[5] N. Nakamoto, T. Takahashi, T. Fukasawa, N. Yoneda, and H. Miyashita, "RCS synthesis of array antenna with circulators and phase shifters and measurement method for deterministic RCS reduction," *IEEE Trans. Antennas Propag.*, vol. 69, no. 1, pp. 135–145, Jan. 2021.

[6] M. Pazokian, N. Komjani, and M. Karimipour, "Broadband RCS reduction of microstrip antenna using coding frequency selective surface," *IEEE Antennas Wireless Propag. Lett.*, vol. 17, no. 8, pp. 1382–1385, Aug. 2018.

[7] J. Yu, W. Jiang, and S. Gong, "Low-RCS beam-steering antenna based on reconfigurable phase gradient metasurface," *IEEE Antennas Wireless Propag. Lett.*, vol. 18, no. 10, pp. 2016–2020, Oct. 2019.

[8] Y. Fan et al., "Low-RCS multi-beam metasurface-inspired antenna based on Pancharatnam–Berry phase," *IEEE Trans. Antennas Propag.*, vol. 68, no. 3, pp. 1899–1906, Mar. 2020.

[9] Y. Liu, W. Zhang, Y. Jia, and A. Wu, "Low RCS antenna array with reconfigurable scattering patterns based on digital antenna units," *IEEE Trans. Antennas Propag.*, vol. 69, no. 1, pp. 572–577, Jan. 2021.

[10] W. He et al., "Investigation of radar cross-section reduction for dihedral corner reflectors based on camouflage grass," *IEEE Antennas Wireless Propag. Lett.*, vol. 20, no. 12, pp. 2447–2451, Dec. 2021.

[11] Q. Wang, X.-Z. Tang, D. Zhou, Z. Du, and X. Huang, "A dual-layer radar absorbing material with fully embedded square-holes frequency selective surface," *IEEE Antennas Wireless Propag. Lett.*, vol. 16, pp. 3200–3203, 2017.

[12] Y. Wang, K. Chen, Y. Li, and Q. Cao, "Design of nonresonant metasurfaces for broadband RCS reduction," *IEEE IEEE Antennas Wireless Propag. Lett.*, vol. 20, no. 3, pp. 346–350, Jan. 2021.

[13] D. Sang, Q. Chen, L. Ding, M. Guo, and Y. Fu, "Design of checkerboard AMC structure for wideband RCS reduction," *IEEE Trans. Antennas Propag.*, vol. 67, no. 4, pp. 2604–2612, Apr. 2019.

[14] Q. Zheng, C. Guo, G. A. E. Vandenbosch, and J. Ding, "Low-profile circularly polarized array with gain enhancement and RCS reduction using polarization conversion EBG structures," *IEEE Trans. Antennas Propag.*, vol. 68, no. 3, pp. 2440–2445, Mar. 2020.

[15] Y. H. Cho and I.-S. Choi, "General mode-matching analysis of a 2-D truncated PEC wedge covered with a magnetodielectric semicircular boss," *IEEE Trans. Antennas Propag.*, vol. 68, no. 12, pp. 8033–8043, Dec. 2020.

[16] T. J. Cui, M. Q. Qi, X. Wan, J. Zhao, and Q. Cheng, "Coding metamaterials, digital metamaterials and programmable metamaterials," *Light, Sci. Appl.*, vol. 3, pp. 1–9, Oct. 2014.

[17] L. H. Gao, Q. Cheng, J. Yang, S. J. Ma, J. Zhao, and S. Liu, "Broadband diffusion of terahertz waves by multi-bit coding metasurfaces," *Light, Sci. Appl.*, vol. 4, no. 9, p. e324, 2015.

[18] Y. Zhao et al., "Broadband low-RCS metasurface and its application on antenna," *IEEE Trans. Antennas Propag.*, vol. 64, no. 7, pp. 2954–2962, Jul. 2016.

[19] Y. Zhao, X. Cao, J. Gao, X. Yao, and X. Liu, "A low-RCS and high-gain slot antenna using broadband metasurface," *IEEE Antennas Wireless Propag. Lett.*, vol. 15, pp. 290–293, 2016.

[20] F. Samadi and A. Sebak, "Wideband, very low RCS engineered surface with a wide incident angle stability," *IEEE Trans. Antennas Propag.*, vol. 69, no. 3, pp. 1809–1814, Mar. 2021.

[21] L. Pósa et al., "A rational fabrication method for low switching-temperature VO_2," *Nanomaterials*, vol. 11, no. 1, p. 212, 2021.

[22] B. Adelaide et al., "Probing relaxation dynamics and stepped domain switching in boron-alloyed VO_2," *Adv. Electron. Mater.*, vol. 8, no. 3, 2022, Art. no. 2100932.